



Influence of defects in graphene on electron transfer kinetics: The role of the surface electronic structure

Vitaliy A. Kislenko ^{a,b}, Sergey V. Pavlov ^{a,b}, Sergey A. Kislenko ^{a,c,*}

^a Joint Institute for High Temperatures of RAS, Izhorskaya 13/2, Moscow, 125412, Russian Federation

^b Skolkovo Institute of Science and Technology, Nobel Str. 3, Moscow, 143026, Russian Federation

^c Moscow Institute of Physics and Technology, Institutskiy per. 9, Dolgoprudny, 141700, Russian Federation



ARTICLE INFO

Article history:

Received 22 December 2019

Received in revised form

16 February 2020

Accepted 2 March 2020

Available online 3 March 2020

Keywords:

Graphene defects

Electron transfer

Quantum capacitance

Selective electrocatalysis

ABSTRACT

The kinetics of an outer-sphere nonadiabatic electron transfer reaction at the defective graphene is theoretically investigated. Different intrinsic and extrinsic point defects were analyzed. The band structure from DFT, in combination with the Gerischer model, was used for the predictions. Calculations were done taking into account the quantum capacitance of the surface for the correct prediction of alignment and occupation of graphene electronic states upon contact with an electrolyte. We have shown that an electrochemical property of graphene largely depends on defect type due to differences in the electronic structure induced by defects. Due to small graphene quantum capacitance, the electron transfer kinetics can be modulated by changes in the double-layer capacitance. The deviations of the potential dependence of the rate constant from the Butler-Volmer kinetics are predicted.

© 2020 Elsevier Ltd. All rights reserved.

1. Introduction

Carbon is widely used in electrochemistry. Graphene, as a new type of carbon-based electrode, provides a great potential for applications in biosensors [1–3] and solar cells [4,5] as well as in many other areas, such as fuel cells, where graphene might be used as a cheap analog of platinum or iridium catalysts [6]. The performance of graphene strongly depends on its chemical structure and electronic properties that have a significant impact on the kinetics of redox processes. Research of heterogeneous electron transfer (ET) at graphene surface is fueled by the new experimental data that indicate a significant change in ET activity at various types of defects, such as vacancies [7], graphene edges [8], nitrogen impurities [9,10], oxygen-containing functional groups [11].

Traditionally, the step edge was considered much more reactive than the basal plane of graphite-based electrodes. A bunch of works claimed that the pristine basal surface of highly oriented pyrolytic graphite (HOPG) has relatively low or even no electroactivity [12,13]. Statements about the inactivity of HOPG basal plane lead to the conclusion that ET occurs only at the ends of carbon nanotubes (CNTs) or graphite/graphene edges [13,14]. However, the

development of new electrochemical methods, such as scanning electrochemical cell microscopy, shows behavior that is more complicated. A freshly cleaved basal surface of HOPG exhibits uniform and high electrochemical activity similar to noble metal electrodes for outer-sphere redox processes [15–17]. However, the activity of the basal plane decreases significantly with time for redox couples with standard potential close to the potential of graphite zero charge due to a spontaneous delamination of the topmost graphene layers from the remainder of the graphite block [18]. At the same time, the aged graphite samples exhibit an enhanced current at the step edges compared to the basal surface. Our resent calculations have revealed that oxygen reduction rate constants above the plane and the edge sites of graphene have nearly the same values due to the strong overlap of donor and acceptor orbitals (adiabatic ET) [19]. Only at long separations (in the nonadiabatic regime) zigzag edges provide faster electron transfer [19,20]. In any case, from a practical perspective, it seems inefficient to utilize only edge sites due to a low edge to plane ratio in the graphene. Thus, other structural imperfections should be used to impart electrocatalytic properties to the whole graphene surface.

As already mentioned, the local electron transfer rate depends on the composition and chemical structure of the surface. Enhanced electrochemical activity for nonadiabatic reactions can be explained by the occurrence of local electronic states within close proximity to the Fermi level [21,22], which lead to larger

* Corresponding author. Joint Institute for High Temperatures of RAS, Izhorskaya 13/2, Moscow, 125412, Russian Federation.

E-mail address: kislenko@ihed.ras.ru (S.A. Kislenko).

overlap between electronic states of graphene and redox couples. It is important to emphasize here that point defects with a predefined concentration, especially mono- and divacancies, can be easily embedded in the basal graphene surface using electron or ion irradiation [23–26]. In this regard, ab initio calculations that allow the effect of various defects on the heterogeneous ET to be assessed become significant.

Herein semi-quantitative analysis of the outer-sphere ET kinetics is performed for the following intrinsic and extrinsic defects: mono- and divacancies, Stone-Wales defect, substitutional nitrogen atom, epoxy (-O-) and hydroxy (-OH) groups. We used the Gerischer model, thus limiting our consideration to nonadiabatic ET. Some aspects of adiabatic electron transfer at the graphene/solution interface have been considered in the theoretical work of Nazmutdinov et al. [27]. Our calculations take into account quantum capacitance of the surface, which is critically important for the correct prediction of levels alignment when the graphene and an electrolyte solution are in contact [28,29]. The main accent is on the interrelation of the ET kinetics and the electronic property changes induced by defects. As was shown by the example of semiconductor CNTs, this is the essential factor by which the ET rate constant can be varied by four orders of magnitude [30].

2. Computational methods

2.1. First-principles calculation

Atomic and band structure calculations were performed using the projector augmented wave (PAW) formalism [31] of density functional theory (DFT) as implemented in Quantum Espresso software package [32,33]. The generalized gradient approximation

2.2. Gerischer model

The analysis of the electron transfer kinetics on the defective graphene surface was carried out in the framework of the Gerischer model, according to which the energy distribution functions of the oxidized and reduced states of a redox couple, $W_{\text{ox}}(E)$ and $W_{\text{red}}(E)$, are described by a Gaussian distribution with a standard deviation of $\sqrt{2\lambda k_B T}$ and means at $E_{F,\text{redox}} + \lambda$ and $E_{F,\text{redox}} - \lambda$ respectively [29,37]:

$$W_{\text{ox}}(E) = \frac{1}{\sqrt{4\pi k_B T \lambda}} \exp \left\{ -\frac{(E - E_{F,\text{redox}} - \lambda)^2}{4k_B T \lambda} \right\} \quad (1)$$

$$W_{\text{red}}(E) = \frac{1}{\sqrt{4\pi k_B T \lambda}} \exp \left\{ -\frac{(E - E_{F,\text{redox}} + \lambda)^2}{4k_B T \lambda} \right\} \quad (2)$$

Where λ is the reorganization energy, $E_{F,\text{redox}}$ is the electrochemical potential of electrons in solution. The electrochemical potential of electrons in an electrolyte relative to a point in vacuum just outside the solution under standard conditions can be calculated from the standard redox potential of a couple V^0 and the absolute potential of the standard hydrogen electrode (SHE) $V_{\text{SHE}}^0(\text{abs})$: $E_{F,\text{redox}} = -|e|(V_{\text{SHE}}^0(\text{abs}) + V^0)$ [38]. The value of $-|e|V_{\text{SHE}}^0(\text{abs})$ was taken equal to -4.5 eV [38,39].

The heterogeneous ET is possible only between states with the same energy. Therefore, the oxidation rate constant is proportional to the product of the density of occupied electronic states $W_{\text{red}}(E)$ in solution and the density of unoccupied states of the electrode $(1 - f(E - E_F + |e|\eta))\rho(E)$ [40–42]:

$$\begin{aligned} k_{\text{ox}} &= \frac{2\pi|H|^2}{\hbar} \Delta z \int_{-\infty}^{\infty} W_{\text{red}}(E) (1 - f(E - E_F + |e|\eta))\rho(E, \eta) dE = \\ &= \frac{2\pi|H|^2}{\hbar \sqrt{4\pi k_B T \lambda}} \Delta z \int_{-\infty}^{\infty} \exp \left\{ -\frac{(E - E_{F,\text{redox}} + \lambda)^2}{4k_B T \lambda} \right\} (1 - f(E - E_F + |e|\eta))\rho(E, \eta) dE = \\ &= \frac{2\pi|H|^2}{\hbar \sqrt{4\pi k_B T \lambda}} \Delta z \cdot k'_{\text{ox}}(\rho, \lambda, \eta) \end{aligned} \quad (3)$$

(GGA) to the exchange-correlation functional in the revised Perdew-Burke-Ernzerhof version (PBEsol) [34] was used. In the geometric optimization and electronic properties calculation the reciprocal space was sampled with $9 \times 9 \times 1$ and $31 \times 31 \times 1$ k-points grids respectively that were generated using the Monkhorst-Pack method [35]. The kinetic energy cutoff for wavefunctions and charge density was 40 Ry and 350 Ry respectively. The total cell energy convergence was no worse than 10^{-5} Ry/cell.

The graphene sheet is modeled with a 10×10 supercell in the lateral direction and with a 1.5 nm vacuum region in the vertical direction. The relatively large lateral supercell was chosen to reduce the interaction between the defect and its periodic images. The optimized graphene lattice constant was 0.2458 nm that is in agreement with the experimental value of 0.246 nm [36].

where H is the electronic coupling element, which is assumed independent on energy; Δz is a narrow range of distances to the surface where the ET is feasible; η is the overpotential; $f(E)$ is the Fermi-Dirac distribution; $\rho(E)$ is the density of electronic states (DOS) of the electrode; E_F is the Fermi energy of the electrode. Since we use a point in vacuum just outside the solution as the energy reference (in accordance with the concept of the absolute electrode potential [43]) the distributions $W_{\text{ox}}(E)$ and $W_{\text{red}}(E)$ don't depend on overpotential, but Fermi distribution $f(E)$ and density of states $\rho(E)$ are biased. Note, that Levich and Dogonadze in the '60s, focusing more on quantum aspects of the ET, used a similar equation to describe electron-transfer reactions at electrodes [44–46].

Similarly, the reduction rate constant is:

$$\begin{aligned}
k_{red} = & \frac{2\pi|H|^2}{\hbar} \Delta z \int_{-\infty}^{\infty} W_{ox}(E) f(E - E_F + |e|\eta) \rho(E, \eta) dE = \\
& \frac{2\pi|H|^2}{\hbar\sqrt{4\pi k_B T \lambda}} \Delta z \int_{-\infty}^{\infty} \exp\left\{-\frac{(E - E_{F,redox} - \lambda)^2}{4k_B T \lambda}\right\} f(E - E_F + |e|\eta) \rho(E, \eta) dE = \\
& \frac{2\pi|H|^2}{\hbar\sqrt{4\pi k_B T \lambda}} \Delta z \cdot k'_{red}(\rho, \lambda, \eta)
\end{aligned} \tag{4}$$

In this work, we focus on the dimensionless integrals $k'_{ox}(\rho, \lambda, \eta)$ and $k'_{red}(\rho, \lambda, \eta)$ of equations (3) and (4) to extract the pure effect of the electronic structure changes caused by the presence of defects on the outer-sphere nonadiabatic ET kinetics.

It should be mentioned that the Gerischer model contains simplifications in which the structure of a reaction layer in solution and distance dependence of the coupling element $H(z)$ are omitted. Earlier, applying molecular dynamics simulation, we showed that the distribution of redox-active components substantially depends on the surface material, its morphology and solvent type [47–50]. In addition to the electronic properties of the surface, the kinetics of ET are also determined by the distribution of reagents and the $H(z)$ dependence [19,51,52]. Therefore, it is important to consider these parameters at the next, more detailed, quantitative analysis of the kinetics.

2.3. Quantum capacitance

Due to the low density of states close to the Fermi energy, graphene exhibits the low quantum capacitance in comparison with the double layer capacitance [53]. This leads to a significant shift of the Fermi level in graphene relative to its band structure upon contact with the electrolyte [28,29]. The total interface capacitance reflects aggregated effect of the quantum (C_Q) and electric double-layer capacitance (C_{EDL}) and can be represented as two series-connected capacitors (Fig. 1a) [28,53].

Fig. 1b illustrates the energy distribution of redox species in solution, as described by equations (1) and (2). The DOS in uncharged defect-free graphene is schematically shown in Fig. 1c. In

general, when the electrode and the electrolyte are not in contact, the Fermi level of the electrode E_F^{vac} is not equal to the Fermi level of the redox couple $E_{F,redox}$. Fig. 1d shows the process of energy alignment during equilibration in the classical limit ($C_Q \gg C_{EDL}$). In this process, the DOS shifts by ΔE_{EDL} as a whole, while the relative population remains unchanged. In the case of the quantum limit ($C_Q \ll C_{EDL}$), the position of the energy bands remains unchanged, while the Fermi level shifts by ΔE_Q to $E_{F,redox}$ (Fig. 1e). In this work, we consider the mixed case when both shifts are taken into account [54]. It can be seen from Fig. 1f that:

$$E_{F,redox} - E_F^{vac} = \Delta E_{EDL} + \Delta E_Q \tag{5}$$

The displacement of the Dirac point ΔE_{EDL} is determined by the electric potential drop $\Delta E_{EDL}/|e|$ across the double layer and can be estimated from the equation:

$$\sigma = -C_{EDL} \Delta E_{EDL}/|e|, \tag{6}$$

where σ is the surface charge density obtained during an equilibration process. C_{EDL} is assumed constant and equal to the typical value of $20 \mu\text{F}/\text{cm}^2$ [53,55,56], unless otherwise stated below.

Since the integral $\int \rho(E)f(E - E_F)dE$ is equal to the number of electrons in a system, the surface charge density is:

$$\begin{aligned}
\sigma = & \frac{|e|}{A} \int \rho(E - \Delta E_{EDL}) \\
& \times [f(E - E_F^{vac} - \Delta E_{EDL}) - f(E - E_F^{vac} - \Delta E_{EDL} - \Delta E_Q)] dE,
\end{aligned} \tag{7}$$

where A is the graphene surface area. Solving Eqs. (5)–(7) one can

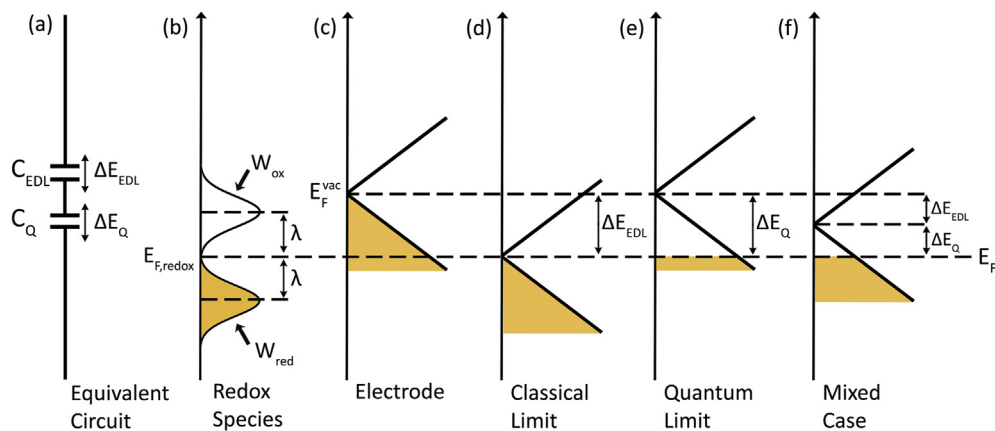


Fig. 1. (a) The equivalent electrical circuit of the capacitance of the graphene/electrolyte interface. (b) The distribution and occupation of redox states in solution. (c) Density and occupation of states in the uncharged graphene. (d–f) The alignment mechanism of Fermi levels in the (d) classical limit, (e) quantum limit, (f) mixed case.

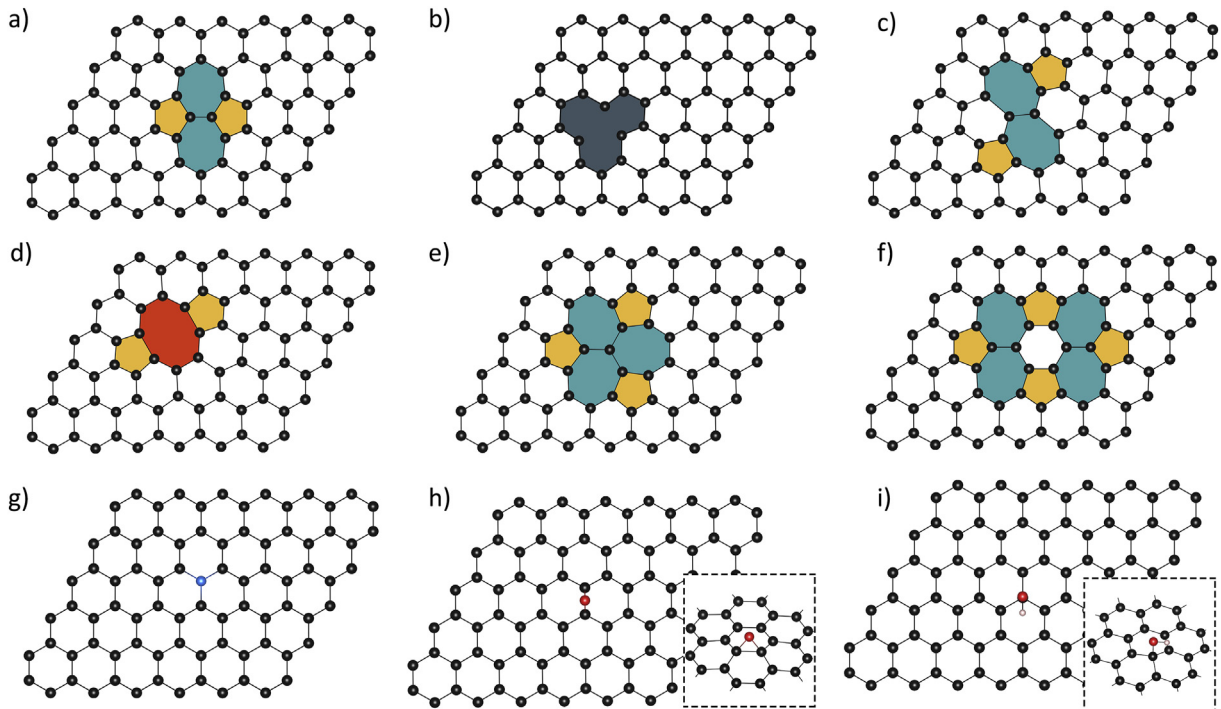


Fig. 2. Relaxed structure of the graphene defects: (a) Stone-Wales defect, (b) monovacancy, (c) DV 55–77, (d) DV 585, (e) DV 555–777, (f) DV 5555–6–7777, (g) substitutional nitrogen impurity, (h) epoxy (-O-) group, (i) hydroxy (OH-) group.

determine the electrochemical potential changes at classical and quantum capacitance (ΔE_{EDL} and ΔE_Q). After that, the ET rate constant can be estimated using Eqs. (3) and (4).

If an overpotential η is applied, the expression (5) takes the form:

$$E_{F,redox} - E_F^{vac} - |e|\eta = \Delta E_{EDL} + \Delta E_Q$$

The Fermi energy of graphene relative to the reference point in vacuum just outside the solid was defined as $E_F^{vac} = E_F - E_{vac}$ [57], where E_{vac} is the vacuum level and E_F is the numerical estimation of the Fermi level. E_F' was selected so that the integral $\int_{-\infty}^{E_F'} \rho(E)dE$ was equal to the number of electrons in the system (see details in Supplementary data, Section S1).

2.4. Defects

We considered several types of intrinsic defects, namely, Stone-Wales defect, monovacancy and several types of divacancies (DV) (Fig. 2). Also, we considered external defects formed by hetero-atoms: substitutional nitrogen atom, epoxy (-O-) and hydroxy (-OH) functional groups (that are largely presented in graphene oxide and reduced graphene oxide [58,59]). Graphene containing the monovacancy, all divacancies and substitutional N is flat. The Stone-Wales defect, -O- and OH- groups lead to the displacement of atoms out of plane and, thereby, create 3D structures. In addition, it is interesting to note the form of the Stone-Wales defect that has the buckled wavelike (sine-like) structure. The maximum out-of-plane displacement is 0.08 nm, which is consistent with the work [60].

3. Results and discussion

3.1. Defective graphene electronic structure

Fig. 3 (f-j, p-t) shows the density of states in graphene with various point defects. It can be seen that the defects can lead to a significant change in electronic properties compared with defect-free graphene. In the case of the monovacancy, DFT calculations predict a high and narrow peak in the density of states near Fermi energy which is consistent with calculations [61] and experiment [21] (Fig. 3h). The Stone-Wales defect and the divacancy 55–77 create a less sharp peak ~0.3–0.8 eV to the right of the Fermi energy (Fig. 3g and i). The divacancy 585 induces the peak, located ~0.25 eV to the right of the Fermi level, that was also observed experimentally [62] (Fig. 3j). The two largest of the considered defects (DV 555–777 and DV 5555–6–7777) also create quite strong DOS perturbations in the Fermi energy region (Fig. 3p, q). The epoxy group has the least effect on the DOS among selected defects (Fig. 3s). In addition, we note that the nitrogen atom, being a donor impurity, leads to a Fermi level shift by 0.3 eV towards higher energies (Fig. 3r, Table S1 in Supplementary data).

To investigate where the defect-induced electronic states are located, the Integrated Local Density of States (ILDOS) was computed. Integration was performed over the interval $[E_F^{vac} - 1 \text{ eV}; E_F^{vac} + 1 \text{ eV}]$. Fig. 3a shows that in the pristine graphene the electron density is equally distributed between all carbon atoms. However, the point defects change this uniform distribution. In the case of the monovacancy, as it is shown in Fig. 3c, the electronic states near the Fermi level are localized directly at the defect. Localization of the defect-induced states are also observed for all divacancies (Fig. 3d, e, k, l), Stone-Wales defect (Fig. 3b),

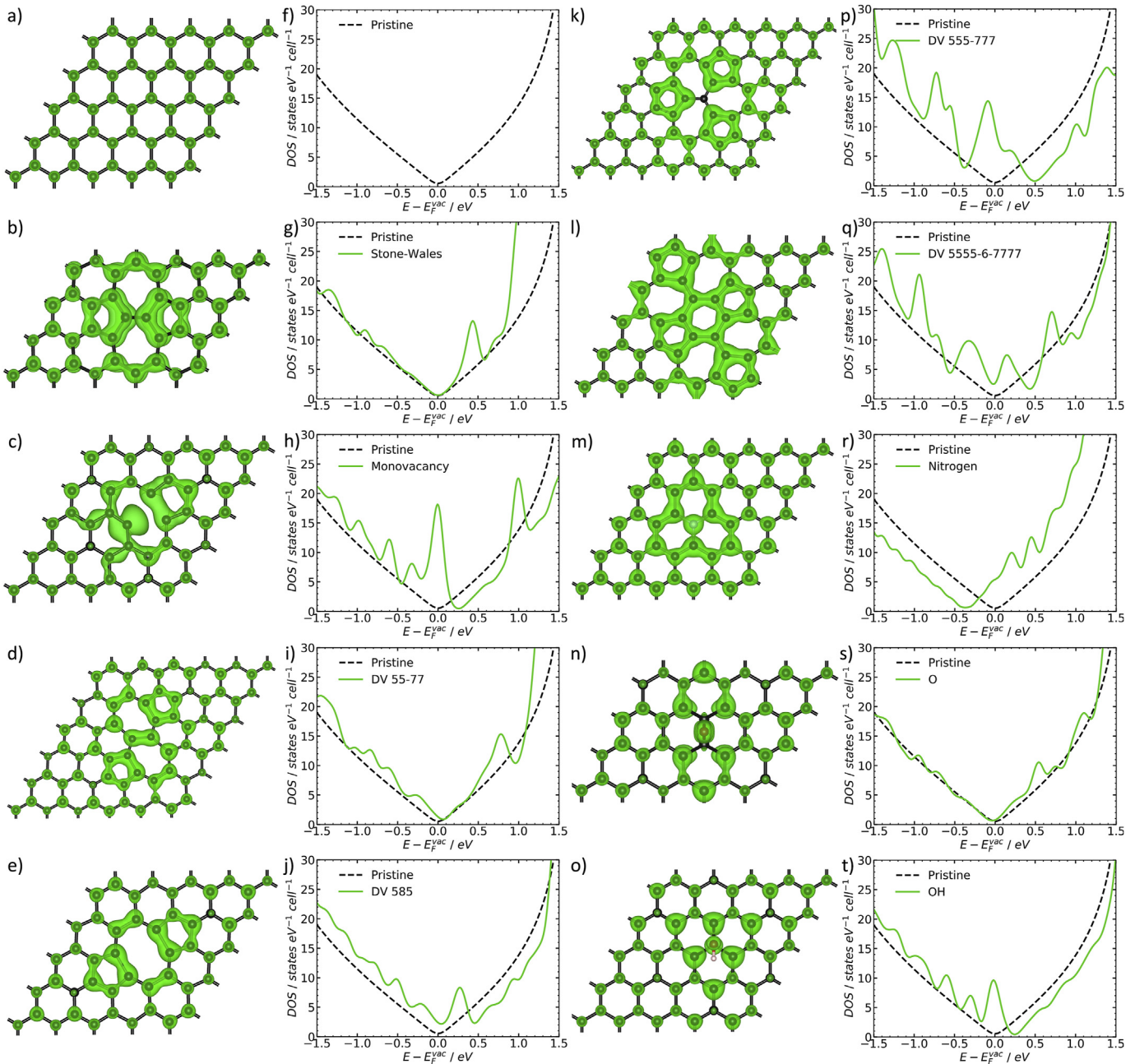


Fig. 3. Integrated local density of states (0.004 e/Bohr³) and density of states of (a, f) Pristine graphene, (b, g) Stone-Wales defect, (c, h) monovacancy, (d, i) DV 55–77, (e, j) DV 585, (k, p) DV 555–777, (l, q) DV 5555–6–7777, (m, r) N (substitutional), (n, s) O (epoxy), (o, t) OH (hydroxy) respectively. To visualize ILDOS iso-surfaces VESTA package was used [63].

substitutional nitrogen impurity (Fig. 3m) and oxygen-containing functional groups (Fig. 3n, o). Consequently, in the nonadiabatic ET regime, the increase in the electrocatalytic activity might be expected in the close proximity of the defect only. Similar spatially dependent heterogeneous electroactivity has been shown for the zigzag graphene edges due to the localization of edge states [19].

3.2. Effect of standard redox potential on the ET rate constant

To evaluate the effect of electronic structure, we calculated the dimensionless standard rate constant of electron transfer $k'_0 = k'_{ox(\eta=0)} = k'_{red(\eta=0)}$ between graphene and a redox couple

depending on the standard redox potential (Fig. 4). The value of the standard redox potential V^0 vs. SHE is depicted by the vertical lines for the most common outer-sphere redox couples [64–66]. As shown in Table S2 in Supplementary data, the reorganization energies for the selected redox couples are around 1 eV. Therefore, the reorganization energy was assumed to be equal to 1 eV in calculations.

The solid black line in Fig. 4 represents the standard rate constant k'_0 of pristine (defect-free) graphene. At $V^0 = -0.2$ V (vs. SHE) the electrochemical potential coincides with the Fermi energy of graphene E_F^{vac} . In this case, $\Delta E_{EDL} = \Delta E_Q = 0$. Hence, the main contribution to the ET is made by levels lying near the Dirac point,

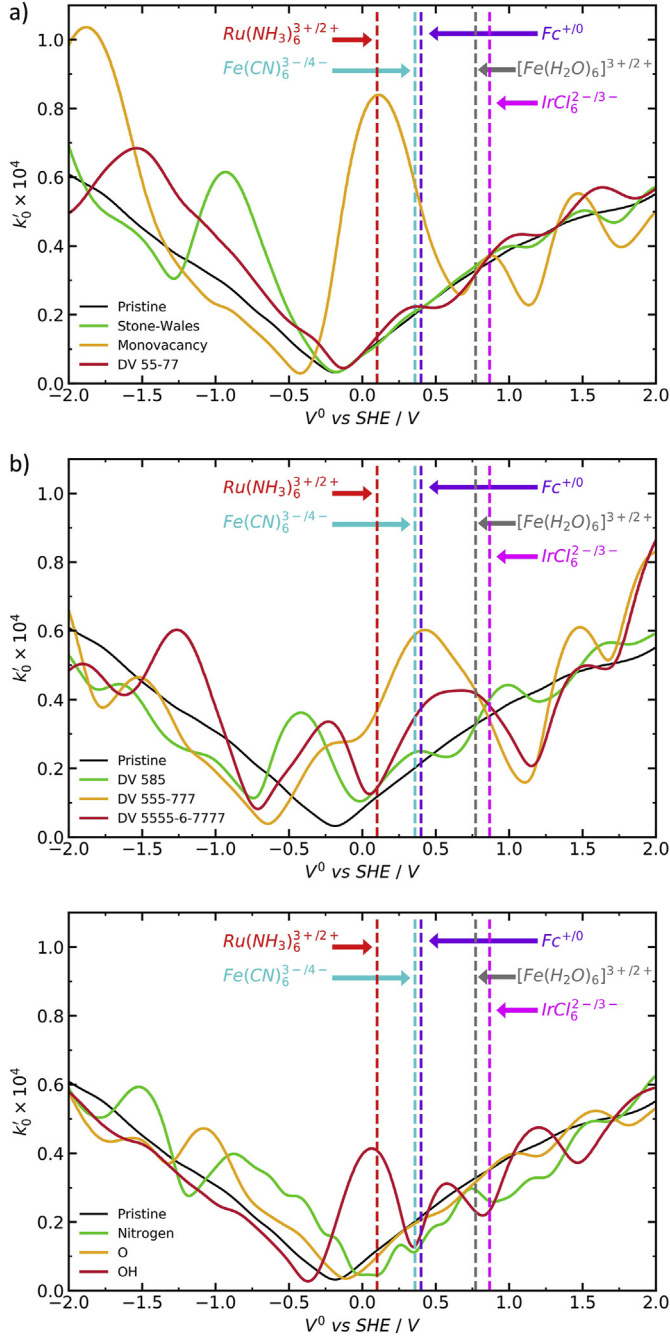


Fig. 4. The dependence of the ET rate constant of defective graphene on the standard redox potential V^0 . The standard potentials for typical one-electron outer-sphere redox couples are depicted by vertical lines [67]. $C_{EDL} = 20 \mu\text{F}/\text{cm}^2$.

where DOS has a minimum (Fig. 3f). Therefore, the rate constant is also minimal. When moving away from the point $V^0 = -0.2$ V, the k'_0 increases in a manner similar to the $\rho(E)$ dependence. It can be explained by the low quantum capacitance of defect-free graphene near the Dirac point. That is why level alignment occurs according to the scenario close to the quantum limit (Fig. 1e).

It can be seen that defects can lead to the catalysis of heterogeneous ET, but the range of standard potentials in which this effect is observed depends on the type of defect. For instance, the monovacancy accelerates the ET by order of magnitude at standard potentials V^0 from -0.2 V to 0.2 V (vs. SHE) (Fig. 4a). It

demonstrates the strongest ET acceleration due to the sharp peak in DOS around the Fermi level (Fig. 3h). The Stone-Wales defect catalyzes ET in another region of standard potentials V^0 from -1.3 to -0.5 V. For redox couples, the standard potential of which lies outside the interval [-1.0 V; 1.0 V], an increase in the rate constant by more than 1.5–2 times in comparison with defect-free graphene is not observed, because a relatively significant rise in the DOS far from the Fermi level cannot be provided by the studied point defects.

A number of experimental results are in agreement with our calculations. For example, the electrocatalytic properties of vacancies were shown in Refs. [7], where an increase in the rate constant by an order of magnitude was found for the FcMeOH^{0/+} redox couple. This effect was obtained when an average distance between defects was ~ 2.5 nm, which is close to our system. For the Ru(NH₃)₆^{3+/2+} redox couple an ET acceleration was shown at graphene edges and with an increase in the number of graphene layers [18]. This effect is explained, on the one hand, by the redox potential of the couple, which lies close to the intrinsic Fermi level of the uncharged graphene, and on the other, by an increase in the density of states near the Fermi level at the edges and with an increase in the number of graphene layers [68]. Since the graphene edges and vacancies increase the DOS near the Fermi level in a very similar way [21,69], we believe that the experiments in Ref. [18] can be considered as indirect support of our calculations that predict catalytic properties of monovacancies for Ru(NH₃)₆^{3+/2+}. In contrast, other redox couples, such as ferrocene derivatives, whose potential is further removed from the intrinsic Fermi level of graphene and graphite, show a uniform and high activity [18]. We also note similar redox-dependent electrochemistry at metal and semiconducting nanotubes [70]. The redox activity of the semiconducting nanotube for Ru(NH₃)₆^{3+/2+} is significantly lower because the redox potential of the couple lies in the band gap. For the oxidation of FcTMA⁺, it is assumed that the Fermi level is shifted out of the band gap that causes a metal-like behavior of the semiconducting nanotube, which is almost indistinguishable from the behavior of the metal one.

Thus, it is possible to rank defects according to their electrocatalytic activity for specific redox reactions. It can be seen that monovacancy provides a higher value of the dimensionless ET rate constant for Ru(NH₃)₆^{3+/2+} and Fe(CN)₆^{3-/4-}. But the rate constant for [Fe(H₂O)₆]^{3+/2+} is higher in the case of divacancy 555–777. Since each defect increases the rate of heterogeneous ET only in a specific range of standard potentials, modifying the surface in a certain way, one can achieve selective activity for a certain redox couple.

3.3. The double-layer capacitance effect on the ET kinetics

Previous results were obtained for a typical value of the double-layer capacitance $C_{EDL} = 20 \mu\text{F}/\text{cm}^2$. As it was shown in the computational details, C_{EDL} determines the Dirac point shift ΔE_{EDL} when two phases are in contact. Thus, along with introducing defects, the electrochemical response can also be tuned by varying the electrical double-layer capacitance. There are several ways to put it into practice, for instance, by changing the electrolyte concentration [56] or by creating non-conductance coatings with variable thickness [71–74].

Fig. 5 demonstrates the effect of the double-layer capacitance on the standard potential dependence of the ET rate constant. Two limiting cases, quantum and classical, in which $C_{EDL} \gg C_Q$ and $C_{EDL} \ll C_Q$ respectively, are also considered. In the classical limit, the electrode band structure is always the same with respect to $E_{F,redox}$ (Fig. 1d). Consequently, the rate constant is independent of V^0

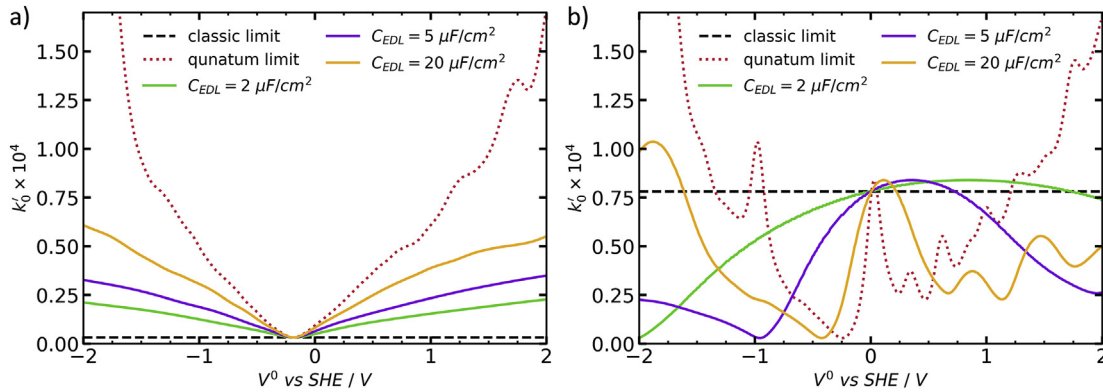


Fig. 5. Effect of the double-layer capacitance on the dependence of the ET rate constant on the standard potential V^0 for (a) pristine graphene and (b) monovacancy.

(Fig. 5). In this case, the DOS near the intrinsic Fermi level of graphene E_F^{vac} determines the non-adiabatic ET rate. Therefore, about 20 times greater k'_0 value for the monovacancy compared to pristine graphene is explained by a proportionally higher DOS near E_F^{vac} (Fig. 3f, h). With the double layer capacitance increase, the quantum capacitance begins to make a more significant contribution. It is reflected in changing of k'_0 on standard redox potential due to a nonzero shift of the electrode Fermi energy relative to the Dirac point. Moreover, the greater C_{EDL} value is, the greater ratio $\Delta E_Q / \Delta E_{EDL}$ is, as it is clearly shown in Fig. 6. In the quantum limit, the dependence of $k'_0(V^0)$ takes a DOS-like shape. Consequently, the width of the region in which monovacancies catalyze ET becomes the narrowest. This effect might be used to control the selectivity of the catalysis of the redox processes.

3.4. Potential dependence of the rate constant

Fig. 7 shows the dependence of the sum of reduction and oxidation rate constants $k'_{red} + k'_{ox}$ on the overpotential η for pristine graphene and graphene with monovacancy. There is also the dependence calculated according to the Butler-Volmer (BV) equation $k'_{red} + k'_{ox} = k'_0(\exp(\alpha\eta/kT) + \exp(-(1-\alpha)\eta/kT))$. The Gerischer model implies that the transfer coefficient α is equal to 0.5 [75]. Thus, this value was used for the evaluation of the BV kinetics.

The results of such calculation for a redox couple whose standard potential is equal to the Fermi energy of uncharged graphene are depicted in Fig. 7a and b. For the pristine graphene, under zero overpotential the Fermi level does not shift and corresponds to the point of minimum DOS. It can be seen that for this case the overpotential dependence of $k'_{red} + k'_{ox}$ is symmetric (Fig. 7a). BV

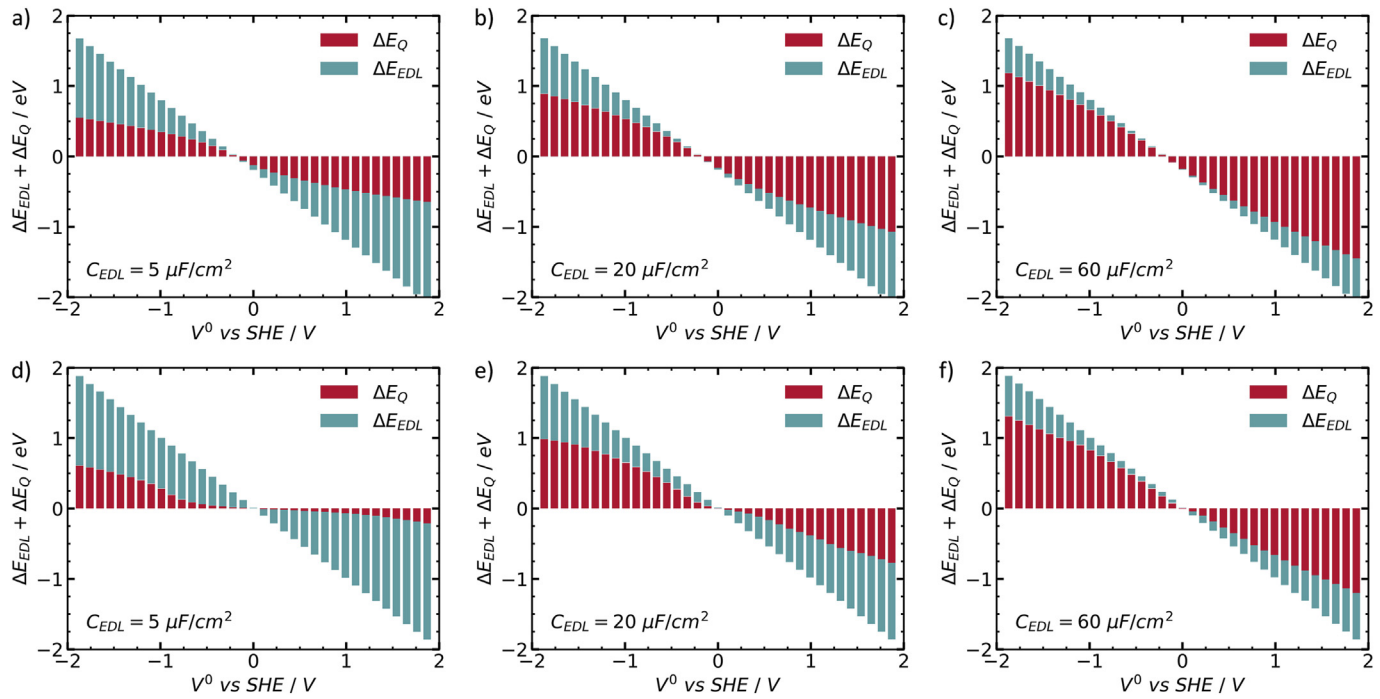


Fig. 6. Relative contributions of quantum and EDL capacitances to the energy bands shift (ΔE_{EDL}) and change in their population (ΔE_Q) in the cases of (a–c) pristine graphene and (d–f) monovacancy.

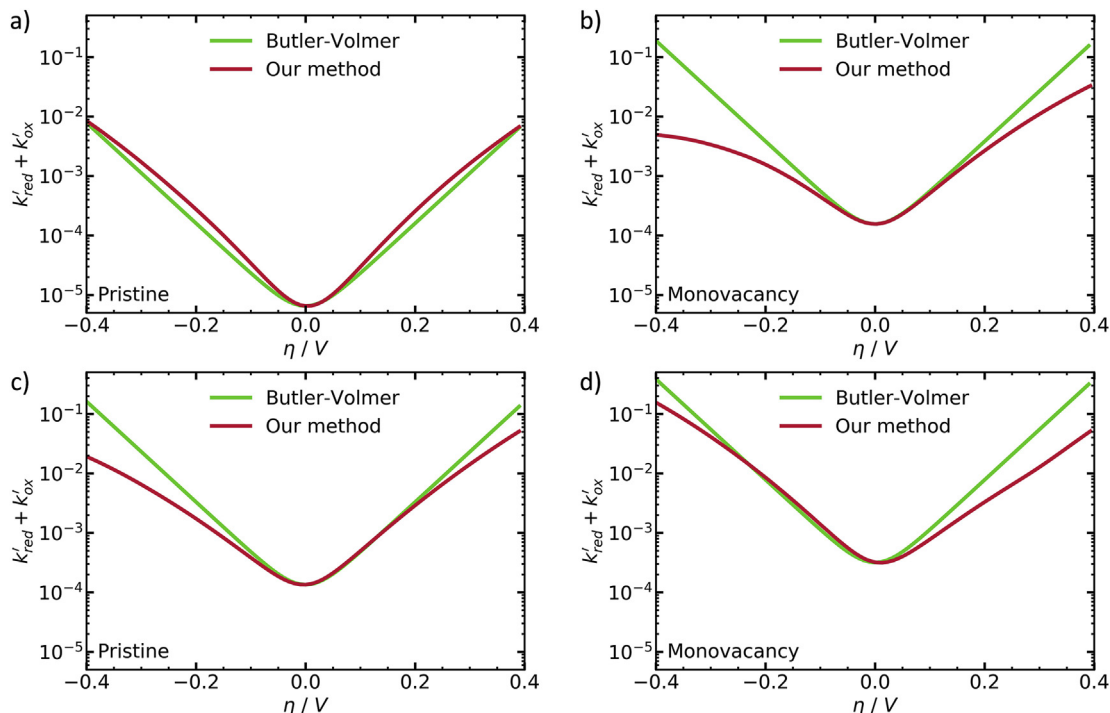


Fig. 7. Potential dependence of $k'_{\text{red}} + k'_{\text{ox}}$ calculated by the Butler-Volmer equation and the Gerischer model with consideration of the quantum capacitance for (a, c) pristine graphene and (b, d) monovacancy. Results in (a) and (b) are for the redox pair whose standard potential is equal to the Fermi energy of the uncharged graphene; (c) and (d) are for $\text{Fc}^{+}/0$.

equation and the method used in this work give close values at low overpotentials.

The results for $\text{Fc}^{+}/0$ redox couple ($V^0 = 0.4 \text{ V}$) is represented in Fig. 7c and d. In this case, the Fermi energy of the pristine graphene at $\eta = 0$ is shifted relative to the point of DOS minimum (Section S3 in Supplementary data). Therefore, at positive overpotentials, the Fermi energy shifts to the region of higher DOS, at negative overpotentials, to the lower DOS region (Fig. S2 in Supplementary info). It leads to the asymmetric dependence of $k'_{\text{red}} + k'_{\text{ox}}$ relative to the point $\eta = 0$; the rate constant is lower at negative overpotentials than at positive (Fig. 7c, Section S3 in Supplementary data). A similar effect is observed for monovacancy in Fig. 7b and d, due to asymmetric DOS with respect to the Fermi level at $\eta = 0$. Thus, a significant deviation from the Butler-Volmer equation is observed.

In a wider range of overpotentials the dependence of $k'_{\text{red}} + k'_{\text{ox}}$ on η has additional features such as local maxima and minima and inflection points that reflect complex DOS structure and Fermi level movement under the influence of quantum capacitance (Fig. S3 in Supplementary data). The existence of the rate constant maximum for pristine graphene at large overpotential was previously observed by Heller et al. [28]. Note also, that considering the specific nature of the DOS of nanoscale electrodes predicts also oscillations of the rate constant at large overpotentials [76].

4. Conclusions

Using the Gerischer model and electronic band structure from DFT calculations, we studied the outer-sphere ET kinetics at graphene with various intrinsic and extrinsic defects, such as mono- and divacancies, Stone-Wales defect, substitutional nitrogen atom, epoxy and hydroxy groups. We focused on the contribution of the graphene electronic structure to the ET rate constant.

It has been shown that the defect induced mid-gap states

catalyze the ET reaction, but the electrochemical response is defect dependent. The most pronounced effect has been observed for the monovacancy for which acceleration of the ET by an order of magnitude with respect to the pristine graphene was predicted for redox couples with standard potentials from -0.2 V to 0.3 V vs. SHE. Due to small quantum capacitance, the electron transfer kinetics can be tuned by the variation of the EDL capacitance from the redox-independent behavior to the DOS-like dependence of the standard rate constant on the redox potential.

We believe that these effects may be useful for applications in selective electrocatalysis and electrochemical sensors. We also consider our results as an important step towards further sophisticated predictions of the ET kinetics with the inclusion of the reactant-surface electronic coupling and the detailed structure of the reaction interface.

Declaration of interest statement

We declare that we have no financial interests or personal relationships that could inappropriately influence the work reported in this paper.

Acknowledgments

We are indebted to prof. R. Nazmutdinov for useful discussions. The work was supported by grant No. 18-03-00773 from the Russian Foundation for Basic Research. The research was carried out using supercomputers at Joint Supercomputer Center of the Russian Academy of Sciences (JSCC RAS) and the equipment of the shared research facilities of HPC computing resources at Lomonosov Moscow State University.

Appendix A. Supplementary data

Supplementary data to this article can be found online at <https://doi.org/10.1016/j.electacta.2020.136011>.

References

- [1] N. Mohanty, V. Berry, Graphene-based single-bacterium resolution biodevice and DNA transistor: interfacing graphene derivatives with nanoscale and microscale biocomponents, *Nano Lett.* 8 (2008) 4469–4476, <https://doi.org/10.1021/nl802412n>.
- [2] Y. Shao, J. Wang, H. Wu, J. Liu, I.A. Aksay, Y. Lin, Graphene based electrochemical sensors and biosensors: a Review, *Electroanalysis* 22 (2010) 1027–1036, <https://doi.org/10.1002/elan.200900571>.
- [3] C. Shan, H. Yang, D. Han, Q. Zhang, A. Ivaska, L. Niu, Graphene/AuNPs/chitosan nanocomposites film for glucose biosensing, *Biosens. Bioelectron.* 25 (2010) 1070–1074, <https://doi.org/10.1016/j.bios.2009.09.024>.
- [4] X. Wang, L. Zhi, K. Müllen, Transparent, conductive graphene electrodes for dye-sensitized solar cells, *Nano Lett.* 8 (2008) 323–327, <https://doi.org/10.1021/nl072838r>.
- [5] P. You, Z. Liu, Q. Tai, S. Liu, F. Yan, Efficient semitransparent Perovskite solar cells with graphene electrodes, *Adv. Mater.* 27 (2015) 3632–3638, <https://doi.org/10.1002/adma.201501145>.
- [6] Y. Jia, L. Zhang, A. Du, G. Gao, J. Chen, X. Yan, C.L. Brown, X. Yao, Defect graphene as a trifunctional catalyst for electrochemical reactions, *Adv. Mater.* 28 (2016) 9532–9538, <https://doi.org/10.1002/adma.201602912>.
- [7] J.-H. Zhong, J. Zhang, X. Jin, J.-Y. Liu, Q. Li, M.-H. Li, W. Cai, D.-Y. Wu, D. Zhan, B. Ren, Quantitative correlation between defect density and heterogeneous electron transfer rate of single layer graphene, *J. Am. Chem. Soc.* 136 (2014) 16609–16617, <https://doi.org/10.1021/ja508965w>.
- [8] W. Yuan, Y. Zhou, Y. Li, C. Li, H. Peng, J. Zhang, Z. Liu, L. Dai, G. Shi, The edge-and basal-plane-specific electrochemistry of a single-layer graphene sheet, *Sci. Rep.* 3 (2013) 2248.
- [9] Y. Li, J. Wang, X. Li, D. Geng, M.N. Banis, R. Li, X. Sun, Nitrogen-doped graphene nanosheets as cathode materials with excellent electrocatalytic activity for high capacity lithium-oxygen batteries, *Electrochim. Commun.* 18 (2012) 12–15, <https://doi.org/10.1016/j.elecom.2012.01.023>.
- [10] H.L. Poh, P. Šimek, Z. Sofer, I. Tomandl, M. Pumera, Boron and nitrogen doping of graphene via thermal exfoliation of graphite oxide in a BF_3 or NH_3 atmosphere: contrasting properties, *J. Mater. Chem. A* 1 (2013) 13146–13153, <https://doi.org/10.1039/C3TA12460F>.
- [11] X. Chia, M. Pumera, Characteristics and performance of two-dimensional materials for electrocatalysis, *Nat. Catal.* 1 (2018) 909–921, <https://doi.org/10.1038/s41929-018-0181-7>.
- [12] T.J. Davies, M.E. Hyde, R.G. Compton, Nanotrench arrays reveal insight into graphite electrochemistry, *Angew. Chem.* 117 (2005) 5251–5256, <https://doi.org/10.1002/ange.200462750>.
- [13] C.E. Banks, T.J. Davies, G.G. Wildgoose, R.G. Compton, Electrocatalysis at graphite and carbon nanotube modified electrodes: edge-plane sites and tube ends are the reactive sites, *Chem. Commun.* (2005) 829–841, <https://doi.org/10.1039/B413177K>.
- [14] C.E. Banks, R.R. Moore, T.J. Davies, R.G. Compton, Investigation of modified basal plane pyrolytic graphite electrodes: definitive evidence for the electrocatalytic properties of the ends of carbon nanotubes, *Chem. Commun.* (2004) 1804–1805, <https://doi.org/10.1039/B406174H>.
- [15] S.C.S. Lai, A.N. Patel, K. McKelvey, P.R. Unwin, Definitive evidence for fast electron transfer at pristine basal plane graphite from high-resolution electrochemical imaging, *Angew. Chem. Int. Ed.* 51 (2012) 5405–5408, <https://doi.org/10.1002/anie.201200564>.
- [16] A.N. Patel, M.G. Collignon, M.A. O'Connell, W.O.Y. Hung, K. McKelvey, J. V Macpherson, P.R. Unwin, A new view of electrochemistry at highly oriented pyrolytic graphite, *J. Am. Chem. Soc.* 134 (2012), <https://doi.org/10.1021/ja308615h>, 20117–20130.
- [17] G. Zhang, A.S. Cuharuc, A.G. Güell, Patrick R. Unwin, Electrochemistry at highly oriented pyrolytic graphite (Hopp): lower limit for the kinetics of outer-sphere redox processes and general implications for electron transfer models, *Phys. Chem. Chem. Phys.* 17 (2015) 11827–11838, <https://doi.org/10.1039/c5cp00383k>.
- [18] A.G. Güell, A.S. Cuharuc, Y.-R. Kim, G. Zhang, S. Tan, N. Ebejer, P.R. Unwin, Redox-dependent spatially resolved electrochemistry at graphene and graphite step edges, *ACS Nano* 9 (2015) 3558–3571, <https://doi.org/10.1021/acsnano.5b00550>.
- [19] S.V. Pavlov, R.R. Nazmutdinov, M.V. Fedorov, S.A. Kislenko, Role of Graphene Edges in the Electron Transfer Kinetics, Insight from theory and molecular modeling, *J. Phys. Chem. C* 123 (2019) 6627–6634, <https://doi.org/10.1021/acs.jpcc.8b12531>.
- [20] S.V. Pavlov, S.A. Kislenko, Graphene electrochemistry: edge vs. basal plane sites, *J. Phys. Conf. Ser.* 1092 (2018) 12112, <https://doi.org/10.1088/1742-6596/1092/1/012112>.
- [21] M.M. Ugeda, I. Brihuega, F. Guinea, J.M. Gómez-Rodríguez, Missing atom as a source of carbon magnetism, *Phys. Rev. Lett.* 104 (2010) 96804, <https://doi.org/10.1103/PhysRevLett.104.096804>.
- [22] H.V. Patten, K.E. Meadows, L.A. Hutton, J.G. Iacobini, D. Battistel, K. McKelvey, A.W. Colburn, M.E. Newton, J.V. Macpherson, P.R. Unwin, Electrochemical mapping reveals direct correlation between heterogeneous electron-transfer kinetics and local density of states in diamond electrodes, *Angew. Chem. Int. Ed.* 51 (2012) 7002–7006, <https://doi.org/10.1002/anie.201203057>.
- [23] O. Lehtinen, J. Kotakoski, A. V Krasheninnikov, A. Tolvanen, K. Nordlund, J. Keinonen, Effects of ion bombardment on a two-dimensional target: atomistic simulations of graphene irradiation, *Phys. Rev. B* 81 (2010) 153401, <https://doi.org/10.1103/PhysRevB.81.153401>.
- [24] O. Lehtinen, J. Kotakoski, A. V Krasheninnikov, J. Keinonen, Cutting and controlled modification of graphene with ion beams, *Nanotechnology* 22 (2011) 175306, <https://doi.org/10.1088/0957-4444/22/17/175306>.
- [25] J. Kotakoski, A.V. Krasheninnikov, U. Kaiser, J.C. Meyer, From point defects in graphene to two-dimensional amorphous carbon, *Phys. Rev. Lett.* 106 (2011) 105505, <https://doi.org/10.1103/PhysRevLett.106.105505>.
- [26] A.W. Robertson, C.S. Allen, Y.A. Wu, K. He, J. Olivier, J. Neethling, A.I. Kirkland, J.H. Warner, Spatial control of defect creation in graphene at the nanoscale, *Nat. Commun.* 3 (2012) 1144.
- [27] R.R. Nazmutdinov, M.D. Bronshtein, E. Santos, Electron transfer across the graphene electrode/solution interface: interplay between different kinetic regimes, *J. Phys. Chem. C* 123 (2019) 12346–12354, <https://doi.org/10.1021/acs.jpcc.9b02164>.
- [28] I. Heller, J. Kong, K.A. Williams, C. Dekker, S.G. Lemay, Electrochemistry at single-walled carbon nanotubes: the role of band structure and quantum capacitance, *J. Am. Chem. Soc.* 128 (2006) 7353–7359, <https://doi.org/10.1021/ja061212k>.
- [29] X. Mao, F. Guo, E.H. Yan, G.C. Rutledge, T.A. Hatton, Remarkably high heterogeneous electron transfer activity of carbon-nanotube-supported reduced graphene oxide, *Chem. Mater.* 28 (2016) 7422–7432, <https://doi.org/10.1021/acs.chemmater.6b03024>.
- [30] S. Kislenko, F. Juarez, F. Dominguez-Flores, W. Schmidkler, R. Nazmutdinov, Tuning the rate of an outer-sphere electron transfer by changing the electronic structure of carbon nanotubes, *J. Electroanal. Chem.* 847 (2019) 113186, <https://doi.org/10.1016/j.jelechem.2019.05.068>.
- [31] G. Kresse, J. Furthmüller, Efficient iterative schemes for ab initio total-energy calculations using a plane-wave basis set, *Phys. Rev. B* 54 (1996) 11169–11186, <https://doi.org/10.1103/PhysRevB.54.11169>.
- [32] P. Giannozzi, S. Baroni, N. Bonini, M. Calandri, R. Car, C. Cavazzoni, D. Ceresoli, G.L. Chiarotti, M. Cococcioni, I. Dabo, A. Dal Corso, S. de Gironcoli, S. Fabris, G. Fratesi, R. Gebauer, U. Gerstmann, C. Goucoussis, A. Kokalj, M. Lazzeri, L. Martin-Samos, N. Marzari, F. Mauri, R. Mazzarello, S. Paolini, A. Pasquarello, L. Paulatto, C. Sbraccia, S. Scandolo, G. Sclauzero, A.P. Seitsonen, A. Smogunov, P. Umari, R.M. Wentzcovitch, Quantum espresso: a modular and open-source software project for quantum simulations of materials, *J. Phys. Condens. Matter* 21 (2009) 395502, <https://doi.org/10.1088/0953-8984/21/39/395502>.
- [33] P. Giannozzi, O. Andreussi, T. Brumme, O. Bunau, M. Buongiorno Nardelli, M. Calandri, R. Car, C. Cavazzoni, D. Ceresoli, M. Cococcioni, N. Colonna, I. Carnimeo, A. Dal Corso, S. de Gironcoli, P. Delugas, R.A. DiStasio, A. Ferretti, A. Floris, G. Fratesi, G. Fugallo, R. Gebauer, U. Gerstmann, F. Giustino, T. Gorni, J. Jia, M. Kawamura, H.-Y. Ko, A. Kokalj, E. Küçükbenli, M. Lazzeri, M. Marsili, N. Marzari, F. Mauri, N.L. Nguyen, H.-V. Nguyen, A. Otero-de-la-Roza, L. Paulatto, S. Poncé, D. Rocca, R. Sabatini, B. Santra, M. Schlipf, A.P. Seitsonen, A. Smogunov, I. Timrov, T. Thonhauser, P. Umari, N. Vast, X. Wu, S. Baroni, Advanced capabilities for materials modelling with Quantum ESPRESSO, *J. Phys. Condens. Matter* 29 (2017) 465901, <https://doi.org/10.1088/1361-648x/aa8f79>.
- [34] J.P. Perdew, A. Ruzsinszky, G.I. Csonka, O.A. Vydrov, G.E. Scuseria, L.A. Constantin, X. Zhou, K. Burke, Restoring the density-gradient expansion for exchange in solids and surfaces, *Phys. Rev. Lett.* 100 (2008) 136406, <https://doi.org/10.1103/PhysRevLett.100.136406>.
- [35] H.J. Monkhorst, J.D. Pack, Special points for Brillouin-zone integrations, *Phys. Rev. B* 13 (1976) 5188–5192, <https://doi.org/10.1103/PhysRevB.13.5188>.
- [36] H. Zhu, P. Huang, L. Jing, T. Zuo, Y. Zhao, X. Gao, Microstructure evolution of diazonium functionalized graphene: a potential approach to change graphene electronic structure, *J. Mater. Chem.* 22 (2012) 2063–2068, <https://doi.org/10.1039/C1JM14862A>.
- [37] R. Memming, Electron transfer theories, *Semicond. Electrochem.*, John Wiley & Sons, Ltd, 2015, pp. 127–169, <https://doi.org/10.1002/978352768865.ch6>.
- [38] R. Memming, Electrochemical systems, *Semicond. Electrochem.*, John Wiley & Sons, Ltd, 2015, pp. 49–60, <https://doi.org/10.1002/978352768865.ch3>.
- [39] A.J. Bard, L.R. Faulkner, *Electrochemical Methods: Fundamentals and Applications*, John Wiley, New York, 2000.
- [40] H. Gerischer, Charge transfer processes at semiconductor-electrolyte interfaces in connection with problems of catalysis, *Surf. Sci.* 18 (1969) 97–122, [https://doi.org/10.1016/0039-6028\(69\)90269-6](https://doi.org/10.1016/0039-6028(69)90269-6).
- [41] H. Gerischer, Über den Ablauf von Redoxreaktionen an Metallen und an Halbleitern: I. Allgemeines zum Elektronenübergang zwischen einem Festkörper und einem Redoxelektrolyten, *Z. Phys. Chem.* 26 (1960) 223–247, https://doi.org/10.1524/zpch.1960.26_3_4.223.
- [42] H. Gerischer, Über den Ablauf von Redoxreaktionen an Metallen und an Halbleitern: II. Metall-Elektroden, *Zeitschrift Fur Physikalische Chemie* 26 (1960) 325–338, https://doi.org/10.1524/zpch.1960.26_5_6.325.
- [43] The absolute electrode potential: an explanatory note (Recommendations 1986), *J. Electroanal. Chem. Interfacial Electrochem.* 209 (1986) 417–428, [https://doi.org/10.1016/0022-0728\(86\)80570-8](https://doi.org/10.1016/0022-0728(86)80570-8).
- [44] V.G. Levich, *Advances in Electrochemistry and Electrochemical Engineering*,

- in: P. Delahay, C.W. Tobias (Eds.) vol. 4, Interscience Publishers, New York; London; Sydney, 1966.
- [45] V.G. Levich, Physical Chemistry: an Advanced Treatise, in: H. Eyring, D. Henderson, W. Jost (Eds.) vol. 9B, Academic Press, New York, 1970.
- [46] R.R. Dogonadze, in: N.S. Hush (Ed.), Reactions of Molecules at Electrodes, J. Wiley, London; New York, 1971.
- [47] S.V. Pavlov, S.A. Kislenko, Effects of carbon surface topography on the electrode/electrolyte interface structure and relevance to Li-air batteries, *Phys. Chem. Chem. Phys.* 18 (2016) 30830–30836, <https://doi.org/10.1039/C6CP05552D>.
- [48] S.A. Kislenko, V.A. Nikitina, R.R. Nazmutdinov, When do defectless alkanethiol SAMs in ionic liquids become penetrable? A molecular dynamics study, *Phys. Chem. Chem. Phys.* 17 (2015) 31947–31955, <https://doi.org/10.1039/C5CP04566E>.
- [49] S.V. Pavlov, S.A. Kislenko, Investigation of the graphene–electrolyte interface in Li-air batteries: a molecular dynamics study, *J. Phys. Conf. Ser.* 946 (2018) 12028, <https://doi.org/10.1088/1742-6596/946/1/012028>.
- [50] S.A. Kislenko, Effect of high donor number solvent and cathode morphology on interfacial processes in Li-air batteries, *J. Phys. Conf. Ser.* 946 (2018) 12029, <https://doi.org/10.1088/1742-6596/946/1/012029>.
- [51] V.A. Nikitina, S.A. Kislenko, R.R. Nazmutdinov, M.D. Bronshtein, G.A. Tsirlina, Ferrocene/ferrocenium redox couple at Au(111)/ionic liquid and Au(111)/acetonitrile interfaces: a molecular-level view at the elementary act, *J. Phys. Chem. C* 118 (2014) 6151–6164, <https://doi.org/10.1021/jp4072108>.
- [52] V.A. Nikitina, S.A. Kislenko, R.R. Nazmutdinov, Understanding the nature of heterogeneous electron transfer in molecular and ionic solvents: experiment, theory, and computations, *J. Phys. Chem. C* 123 (2019) 14370–14381, <https://doi.org/10.1021/acs.jpcc.9b01163>.
- [53] C. Zhan, J. Neal, J. Wu, D. Jiang, Quantum effects on the capacitance of graphene-based electrodes, *J. Phys. Chem. C* 119 (2015) 22297–22303, <https://doi.org/10.1021/acs.jpcc.5b05930>.
- [54] S. Sun, Y. Qi, T.-Y. Zhang, Dissecting graphene capacitance in electrochemical cell, *Electrochim. Acta* 163 (2015) 296–302, <https://doi.org/10.1016/j.electacta.2015.02.049>.
- [55] T. Pajkossy, D.M. Kolb, Double layer capacitance of the platinum group metals in the double layer region, *Electrochim. Commun.* 9 (2007) 1171–1174, <https://doi.org/10.1016/j.elecom.2007.01.002>.
- [56] J. Xia, F. Chen, J. Li, N. Tao, Measurement of the quantum capacitance of graphene, *Nat. Nanotechnol.* 4 (2009) 505–509, <https://doi.org/10.1038/nano.2009.177>.
- [57] M. Legesse, F. El Mellouhi, E.T. Bentria, M.E. Madjet, T.S. Fisher, S. Kais, F.H. Alharbi, Reduced work function of graphene by metal adatoms, *Appl. Surf. Sci.* 394 (2017) 98–107, <https://doi.org/10.1016/j.apsusc.2016.10.097>.
- [58] K. Krishnamoorthy, M. Veerapandian, K. Yun, S.-J. Kim, The chemical and structural analysis of graphene oxide with different degrees of oxidation, *Carbon N. Y.* 53 (2013) 38–49, <https://doi.org/10.1016/j.carbon.2012.10.013>.
- [59] A. Bagri, C. Mattevi, M. Acik, Y.J. Chabal, M. Chhowalla, V.B. Shenoy, Structural evolution during the reduction of chemically derived graphene oxide, *Nat. Chem.* 2 (2010) 581–587, <https://doi.org/10.1038/nchem.686>.
- [60] J. Ma, D. Alfe, A. Michaelides, E. Wang, Stone-Wales defects in graphene and other planar sp²-bonded materials, *Phys. Rev. B* 80 (2009) 33407, <https://doi.org/10.1103/PhysRevB.80.033407>.
- [61] T.O. Wehling, S. Yuan, A.I. Lichtenstein, A.K. Geim, M.I. Katsnelson, Resonant scattering by realistic impurities in graphene, *Phys. Rev. Lett.* 105 (2010) 56802, <https://doi.org/10.1103/PhysRevLett.105.056802>.
- [62] M.M. Ugeda, I. Brihuega, F. Hiebel, P. Mallet, J.-Y. Veilhan, J.M. Gómez-Rodríguez, F. Ynduráin, Electronic and structural characterization of divacancies in irradiated graphene, *Phys. Rev. B* 85 (2012) 121402, <https://doi.org/10.1103/PhysRevB.85.121402>.
- [63] K. Momma, F. Izumi, VESTA 3 for three-dimensional visualization of crystal, volumetric and morphology data, *J. Appl. Crystallogr.* 44 (2011) 1272–1276, <https://doi.org/10.1107/S0021889811038970>.
- [64] L.M. Torres, A.F. Gil, L. Galicia, I. González, Understanding the difference between inner- and outer-sphere mechanisms: an electrochemical experiment, *J. Chem. Educ.* 73 (1996) 808, <https://doi.org/10.1021/ed073p808>.
- [65] D.M. Murphy, R.J. Cullen, D.R. Jayasundara, R.L. Doyle, M.E.G. Lyons, P.E. Colavita, Heterogeneous charge transfer at the amorphous carbon/solution interface: effect on the spontaneous attachment of aryl diazonium salts, *J. Phys. Chem. C* 117 (2013) 22768–22777, <https://doi.org/10.1021/jp406686e>.
- [66] K. Slowinski, K.U. Slowinska, M. Majda, Electron tunneling across hexadecanethiolate monolayers on mercury Electrodes: reorganization energy, structure, and permeability of the alkane/water interface, *J. Phys. Chem. B* 103 (1999) 8544–8551, <https://doi.org/10.1021/jp991466a>.
- [67] W.M. Haynes, CRC Handbook of Chemistry and Physics, CRC Press, 2017.
- [68] P.R. Unwin, A.G. Güell, G. Zhang, Nanoscale electrochemistry of sp² carbon materials: from graphite and graphene to carbon nanotubes, *Acc. Chem. Res.* 49 (2016) 2041–2048, <https://doi.org/10.1021/acs.accounts.6b00301>.
- [69] Y. Niimi, T. Matsui, H. Kambara, K. Tagami, M. Tsukada, Hiroshi Fukuyama, Scanning tunneling microscopy and spectroscopy of the electronic local density of states of graphite surfaces near monoatomic step edges, *Phys. Rev. B* 73 (2006), 085421, <https://doi.org/10.1103/PhysRevB.73.085421>.
- [70] A.G. Güell, K.E. Meadows, P. V Dudin, N. Ebejer, J. V Macpherson, P.R. Unwin, Mapping nanoscale electrochemistry of individual single-walled carbon nanotubes, *Nano Lett.* 14 (2014) 220–224, <https://doi.org/10.1021/nl403752e>.
- [71] B. Lee, Y. Chen, F. Duerr, D. Mastrogiovanni, E. Garfunkel, E.Y. Andrei, V. Podzorov, Modification of electronic properties of graphene with self-assembled monolayers, *Nano Lett.* 10 (2010) 2427–2432, <https://doi.org/10.1021/nl100587e>.
- [72] C. Yan, K.-S. Kim, S.-K. Lee, S.-H. Bae, B.H. Hong, J.-H. Kim, H.-J. Lee, J.-H. Ahn, Mechanical and environmental stability of polymer thin-film-coated graphene, *ACS Nano* 6 (2012) 2096–2103, <https://doi.org/10.1021/mn203923n>.
- [73] B. Long, M. Manning, M. Burke, B.N. Szafranek, G. Visimberga, D. Thompson, J.C. Greer, I.M. Povey, J. MacHale, G. Lejosne, D. Neumaier, A.J. Quinn, Non-covalent functionalization of graphene using self-assembly of alkane-amines, *Adv. Funct. Mater.* 22 (2012) 717–725, <https://doi.org/10.1002/adfm.201101956>.
- [74] H. Yan, X. Li, B. Chandra, G. Tulevski, Y. Wu, M. Freitag, W. Zhu, P. Avouris, F. Xia, Tunable infrared plasmonic devices using graphene/insulator stacks, *Nat. Nanotechnol.* 7 (2012) 330–334, <https://doi.org/10.1038/nnano.2012.59>.
- [75] S. Chen, Y. Liu, J. Chen, Heterogeneous electron transfer at nanoscopic electrodes: importance of electronic structures and electric double layers, *Chem. Soc. Rev.* 43 (2014) 5372–5386, <https://doi.org/10.1039/C4CS00087K>.
- [76] H. Yamada, R. Narayanan, P.R. Bandaru, Electrochemical kinetics and dimensional considerations at the nanoscale: the influence of the density of states, *MRS Commun.* 7 (2017) 651–657, <https://doi.org/10.1557/mrc.2017.93>.